Contents lists available at ScienceDirect

Transactions of Nonferrous Metals Society of China

36(2026) 488−506

www.tnmsc.cn

Effect of laser remelting on microstructure and properties of Ti6Al4V titanium alloy prepared by laser powder bed fusion

Yue-yang LIU [a], Yang YANG [a,*], Xiang CHEN [b], Yu-xing ZHAN [a]

[a] School of Materials Science and Engineering, Central South University, Changsha 410083, China;

[b] State Key Laboratory of Precision Blasting, Jianghan University, Wuhan 430056, China

Abstract: Laser remelting (LR) was used as an auxiliary post-treatment process for the Ti6Al4V titanium alloys fabricated by laser powder bed fusion (LPBF). Optical microscope (OM), scanning electron microscope (SEM) and electron back scattering diffraction (EBSD) observations showed that the grains in melted zone (MZ) transformed into equiaxial grains with an average size of 1.31 μm, and the grains in heat affected zone (HAZ) were refined. Moreover, the texture intensity dropped significantly from 13.86 to 6.35 in MZ and 10.79 in HAZ. The temperature gradient (G) to solidification rate (R) ratio decreased when the laser scanning speed slowed down to a certain extent in the LR process, which effectively improved the highly preferred orientation and filled the hole defects in the surface of LPBF-Ti6Al4V. Furthermore, the hardness, wear resistance and corrosion resistance of the surface of the LPBF samples were improved by LR treatment.

Keywords: laser powder bed fusion; laser remelting; grain refinement; preferred orientation; wear behavior; electrochemical properties; Ti6Al4V

1 Introduction

Laser powder bed fusion (LPBF), also known as selective laser melting (SLM), is an additive manufacturing technology that utilizes a laser beam as the energy source and alloy powder as the raw material for layer-by-layer formation [1−3]. LPBF is a technology with considerable development potential and is widely used in the domains of mechanical engineering and biomedicine due to its fast speed, high precision, and near-net-shaping properties [4−7]. Ti6Al4V alloy, a typical α+β duplex alloy, is widely used in aerospace, oceanic, and biomedical applications due to its high specific strength, excellent ductility, outstanding corrosion resistance, and remarkable biocompatibility. Specialized equipment is required for the traditional process of Ti6Al4V alloy because of the high energy consumption and material waste [8,9]. In recent decades, researchers have increasingly focused on the titanium alloys and additive manufacturing. The Ti6Al4V alloys produced by the LPBF technology demonstrate remarkable superiority in the fabrication of patient-specific medical implants and aircraft components [10].

However, the presence of the high cooling rate (above 10^4 K/s) and significant temperature gradient (above 10^4 K/m) in the melt pool during LPBF [11] is not conducive to the complete fusion of the powder and is prone to the formation of defects, such as holes and porosity. Based on the model proposed by MERCELIS and KRUTH [12], the internal residual stress field of LPBF was influenced by its multi-pass and cyclic process of melting and subsequent solidification. The non-

Corresponding author: *Yang YANG, Tel: +86-15874219683, E-mail: yangyang@csu.edu.cn, yangyanggroup@163.com

https://doi.org/10.1016/S1003-6326(25)66977-9

Received 8 May 2024; accepted 26 December 2024

uniform thermal expansion and contraction process between passes results in residual tensile stress in the surface layer of the formed material, which negatively affects the overall mechanical properties of the alloys [13]. In the LPBF process, interlayer heat conduction is evident. A pronounced temperature gradient is formed due to the relatively low temperature of the powder during the printing of the initial layer. However, the temperature gradient gradually diminishes as the number of printed layers increases. The growth of the dendritic grains exhibits an obvious preferential orientation in such complex temperature field conditions, leading to variations in the performance of printed parts along different directions. For example, the fatigue life in the direction of construction is significantly longer compared to that in the horizontal direction [14,15]. In summary, LPBF-fabricated components may exhibit residual tensile stresses, pronounced preferential orientations, incomplete powder fusion, porosity, and other associated issues. These factors severely compromise the fatigue performance, corrosion resistance, and service life of LPBF products, thereby greatly hindering their potential application in engineering.

Significant research efforts have been devoted to improving the microstructure and optimizing the residual stress state of the surface layer in components produced by LPBF. Currently, various methods including in-situ heating [16,17], heat treatment [18], rolling [19,20], and mechanical shot peening [21] have been developed to enhance the microstructure and optimize the distribution of residual stresses. However, these methods still exhibit limitations in terms of altering the final shape and size of the nearly finalized printed components.

A high-energy laser beam is utilized as the energy source to rapidly elevate the surface layer of the original material to the liquefaction temperature, thereby forming a new melt pool on the surface of material and effectively filling in the pre-existing pore defects in the LR process. Meanwhile, heat is diffused to the surrounding environment and the low-temperature substrate through convection and conduction. Due to the lower ambient and substrate temperatures in LPBF processes, as well as the higher thermal diffusivity of solid materials compared to powders, there is a significant undercooling of the remelted surface layer during the laser remelting (LR) process. The nucleation rate in the melt pool is notably enhanced, resulting in grain sizes significantly smaller than those achieved through the LPBF process alone [22]. Furthermore, the convective heat transfer during the remelting treatment on the surface is straightforward, as it involves only a single-layer melting−solidification process. A solidification mode akin to planar development is established, thereby preventing the phenomenon of pronounced selective orientation [23]. ZHANG et al [24] carried out laser remelting treatment on Mg−3Nd−1Gd−0.5Zr (EV31) alloy and obtained refined equiaxed grains. MUKHERJEE et al [25] used a pulsed laser beam to remelt the surface of Ti6Al4V alloy, and simulated corrosive environment tests were carried out on the obtained corrugated surface, showing that the remelting treatment could significantly improve the corrosion and friction wear resistance of Ti6Al4V alloy. LIEN et al [26] used laser remelting to create three distinct types of Al−Si eutectic, investigating the alteration mechanism of Al−20Si alloy at various scanning speeds. Currently, there is a scarcity of research on the application of laser remelting as a supplementary post-treatment method for LPBF. Limited investigations have been carried out on the kinetics of phase transformation, grain growth, crystal texture, and property evolution in LPBF-Ti6Al4V alloy, particularly under the rapid cooling rates experienced during laser remelting.

To address issues such as incomplete melting of powder, pores, relatively large grain size, and performance anisotropy caused by laser powder bed fusion (LPBF), the laser remelting post-treatment process was innovatively used to modify the surface microstructure and performance of the LPBF-Ti6Al4V alloy in this work. A systematic investigation was conducted to examine the impact of laser remelting on the microstructure and properties of LPBF-Ti6Al4V alloy, offering a novel approach to further enhance the overall performance of the titanium alloy produced by additive manufacturing.

2 Experimental

2.1 Preparation of Ti6Al4V samples by LPBF

The Ti6Al4V powder, sourced from Wuxi

Feier Kang Company, was utilized as the raw material in the LPBF process. The powder exhibited a spherical morphology (Fig. 1(a)) and had a median particle size of 33.0 μm (Fig. 1(b)). The chemical composition of the raw material is presented in Table 1.

The Farsoon 271M system was utilized to introduce argon gas into the molding chamber, ensuring that the oxygen content in the chamber remained below 0.02%. The Ti6Al4V powder was pre-layered onto the titanium substrate and preheated to 150 °C, and then the printing work was started with the substrate surface defined as the *XOY* surface and the *Z* direction as the build direction. The printing process is shown in Fig. 2. After preparation, the substrate was slowly cooled down to room temperature in 2 h. The laser power was adjusted to be 225 W, and the powder thickness of each layer was kept at 30 μm. The scanning speed was 1000 mm/s and the pitch of each scan was 120 μm.

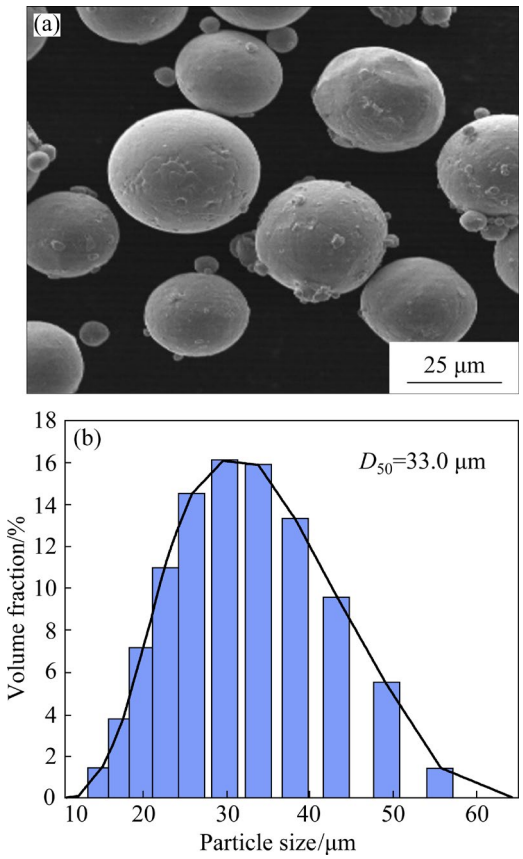

Fig. 1 (a) Ti6Al4V powder morphology; (b) Powder particle size distribution

Table 1 Chemical composition of Ti6Al4V powder (wt.%)

Al	V	Fe	N	H	O	Ti
6.08	4.04	0.043	0.0027	0.0008	0.956	Bal.

The energy density was calculated by the following equation [27]:

$$D_{VE} = \frac{P}{v_s th} \quad (1)$$

where D_{VE} denotes the volumetric energy density (J/mm^2), P is the laser beam power (W), v_s is the scanning speed of the laser beam (mm/s), t is the thickness of the powder layer, and h is the distance of the scanning channel. The D_{VE} was calculated to be 62.5 J/mm^2 for the LPBF process.

2.2 Laser remelting

LR was carried out using the DILAS semi-conductor (model E15.4B3-980-IS27.5) with an optical output of 3 kW, a focal length of 370 mm, and a wavelength of (980±10) nm. The laser system

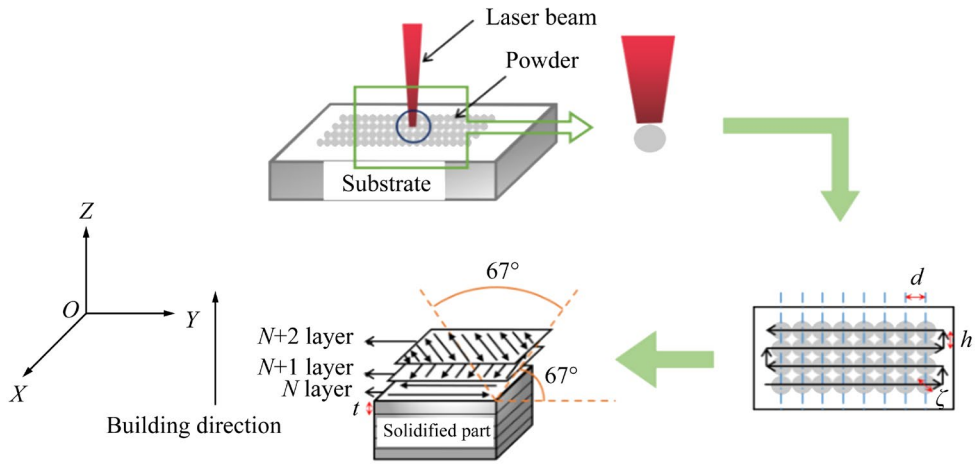

Fig. 2 LPBF scanning strategy

was operated at a standard current of 78 A and voltage of 78 V under an argon atmosphere for protection, with a laser power of 1 kW. The scanning speed was set at 20 mm/s, spot diameter was maintained at 4 mm, and lap rate was set to be 50%. The reciprocating S-shaped scanning strategy [28], as depicted in Fig. 3, was adopted for the scanning process.

The laser energy density could be expressed as [29]

$$E=\frac{P}{v\xi} \tag{2}$$

where E is the energy density (J/mm^2), v is the laser beam traveling speed (mm/s), and ξ is the spot size (mm). It was calculated that E=12.5 J/mm^2 in this experiment.

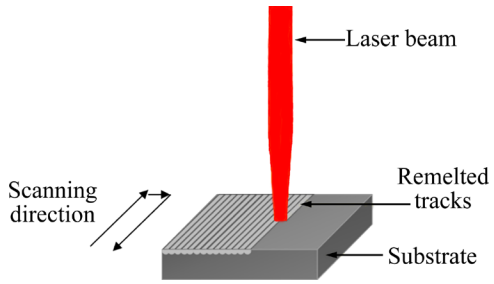

Fig. 3 Scanning strategy for laser remelting process

2.3 Material characterization

The microstructure of LRed samples was observed by OM, SEM and EBSD.

The Kroll reagent, which was composed of 2 vol.% HF, 3 vol.% HCl, 5 vol.% HNO_3, and 90 vol.% H_2O, was used to corrode the samples for 55 s after they were polished and ground. The samples were observed by Leica metallographic microscope DM2700M.

The Cu K_α (λ=1.54 Å) was chosen for scanning at a rate of 8 (°)/min using an X-ray diffractometer model D/max 2550, which was used to analyze the Ti6Al4V alloy. Jade software was utilized to analyze the X-ray diffraction data and determine the phase.

Stainless steel sheet was used as the cathode material in this research. 95 mL glacial acetic acid and 5 mL perchloric acid were combined to yield the electrolyte solution used for the electrolytic polishing of the LPBF and LRed Ti6Al4V alloys. Following ultrasonic cleaning, ultra-high resolution large beam cold field emission scanning electron microscopy (Hitachi/Regulus8230) was used to perform EBSD experiments on the two samples at a scanning step of 0.2 μm. OimA software was used to examine the grain size and texture intensity of the test areas.

2.4 Performance tests

2.4.1 Microhardness test

The hardness variations in the as-deposited LPBF and LRed Ti6Al4V titanium alloys were investigated by microhardness measurements. The HV−1000Z digital Vickers microhardness tester was used to set the applied load at 0.2 kg (equivalent to 1.96 N), with a load retention time of 15 s, and 6 points were probed simultaneously and their average value was calculated.

2.4.2 Electrochemical test

A MULTI AUTOLAB M204 multichannel electrochemical workstation from the Netherlands was used for the impedance tests and polarization curve measurements. A three-electrode system was built in the setup, where the Ti6Al4V specimen served as the working electrode, a platinum sheet acted as the auxiliary electrode, and a saturated calomel electrode (SCE) was used as the reference electrode. The sample with a surface area of 1.0 cm^2 was kept in 3.5 wt.% NaCl solution for enough time to obtain a stable open-circuit potential (OCP). At the room temperature, the scanning range and rate for the potentio-dynamic polarization (PDP) test were set from −1.0 to 1.0 V and at 0.6 mV/s, respectively. The frequency range, code and amplitude for the test of the electrochemical impedance spectroscopy (EIS) were set at 10^{-2}−10^5 HZ, sinusoidal and 10 mV, respectively.

2.4.3 Friction and wear test

The wear resistances of the LPBF-Ti6Al4V and LRed-Ti6Al4V samples were tested using an HT−600 high-temperature friction and wear machine. A cubic silicon nitride ball with a diameter of 6 mm, a load of 20 N, a wear radius of 8 mm, and a duration of 30 min was used as the grinding material.

3 Results and discussion

3.1 Influence of LR on microstructure of LPBF-Ti6Al4V titanium alloy

3.1.1 Phases constitution

The XRD patterns of the LPBF and LRed titanium alloys were presented in Fig. 4. It was

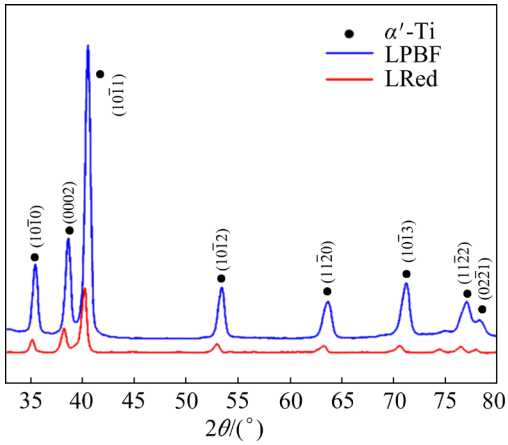

Fig. 4 X-ray diffraction patterns of surface of LPBF-Ti6Al4V and LRed-Ti6Al4V alloys

evident that both samples primarily exhibited α (α') phases, as there were no significant changes in the positions of all peaks observed in the diffraction pattern. According to the Bragg's law, the lattice parameters, a and c, of the LPBF-Ti6Al4V were (2.928033±0.0012) Å and (4.665073±0.0021) Å, while the lattice parameters, a and c, of the LRed-Ti6Al4V were (2.943186±0.0015) Å and (4.698573±0.0020) Å, respectively. The calculated results of two samples were basically consistent with the lattice parameter of α/α' phase (a=2.92 Å, and c=4.63 Å) in the standard PDF (powder diffraction file) (No. 44-1294), with no noticeable β peaks observed in the XRD pattern. Thus, it could be assumed that both samples were composed of the α (α') phase. It was deemed impractical to differentiate between the α and α' phase solely through X-ray diffraction analysis, owing to their identical microstructural characteristics and lattice parameters. Therefore, the consideration of the manufacturing process features became imperative [30,31]. Both samples underwent the processes involving rapid heating, melting, and subsequent cooling solidification, wherein the cooling rate exceeded 10^4 K/s [30]. The original β phase was not able to transform into α phase, which could only perform a non-diffusion-type phase transformation into α' martensitic phase [31]. Consequently, it could be concluded that both LPBF and LRed Ti6Al4V alloys were composed of α' phases with hexagonal close packed structure in this experiment.

From Fig. 4, it could be found that there was an obvious strongest peak (10$\bar{1}$1) in the XRD patterns of the original LPBF-Ti6Al4V and LRed-Ti6Al4V, which indicated that there was a preferred orientation in the material in (10$\bar{1}$1) diffraction direction. In order to show the degree of preferred orientation, the method in literature [32,33] was adopted. Initially, it was assumed that the peak intensities at the respective (10$\bar{1}$1) positions for the standard PDF card, LPBF and LRed-Ti6Al4V were 100 respectively. Then, the relative peak intensities of the remaining main peaks of the standard PDF card and different samples relative to the main peak (10$\bar{1}$1) were calculated, respectively (For instance, if the absolute peak intensity value of (10$\bar{1}$0) in the standard card is 25.10% that of (10$\bar{1}$1), then the relative peak intensity value of (10$\bar{1}$0) was 25.10 and so on for others). Finally, the degree of preferred orientation was evaluated by comparing the magnitudes of the differences between the relative peak intensities of the other main peaks except (10$\bar{1}$1) of the LPBF and LRed-Ti6Al4V samples and the relative peak intensities of the standard cards. The larger the difference, the more obvious the preferred orientation. The calculated data were presented in Table 2. It could be seen that the peak intensities of the diffraction peaks of the LRed-Ti6Al4V distributed more evenly, indicating a more homogeneous grain orientation in it.

Table 2 Comparison of relative peak intensity of main peak (except for (10$\bar{1}$1)) of LPBF-Ti6Al4V and LRed-Ti6Al4V samples with standard card

Main peak	Relative peak intensity of standard card/%	LRed-Ti6Al4V		LPBF-Ti6Al4V	
		Relative peak intensity/%	Difference from standard card/%	Relative peak intensity/%	Difference from standard card/%
(10$\bar{1}$0)	25.10	25.36	0.26	26.21	1.11
(0002)	25.50	34.86	9.36	52.38	26.88
(10$\bar{1}$2)	13.30	14.54	1.24	17.68	4.38
(11$\bar{2}$0)	14.50	13.00	1.50	12.97	1.53

The results presented in Table 2 indicated that the relative peak strengths of the main peaks in the LRed-Ti6Al4V were closer to the standard value than the LPBF-Ti6Al4V, which proved that the preferred orientation phenomenon was significantly reduced. Different from the multi-pass thermal cycle process during LPBF, where heat conduction between layers was inevitable, the LR process only took place once in the surface, avoiding the occurrence of heat conduction between layers. Additionally, the Ti6Al4V sample demonstrated a higher temperature gradient during the process of LPBF. It was attributed to the slower and more uneven coefficient of thermal conductivity of the powder, in contrast to the solid material formed during the LR process. As a result, heat dissipation in various directions was also notably different. As a result, the grains in LPBF-Ti6Al4V grew along the direction of the maximum heat flux, leading to the formation of epitaxial columnar grains [34]. The LR process modified the microstructure by altering the direction of maximum heat flux on the alloy surface, thereby mitigating the anisotropic issue in the LPBF-Ti6Al4V.

3.1.2 Effect of LR on morphology

The morphology of the *YOZ* surface of the LPBF-Ti6Al4V was presented in Fig. 5. In Fig. 5(a), it was indicated that there were obvious hole defects within the LPBF-Ti6Al4V, which would reduce the sample densification and take an impact on the overall mechanical properties [35], which were supposed to be the result of the insufficient melting of powder and the presence of remaining gas during the LPBF process. As illustrated in Fig. 5(b), the β phase grain boundaries were found to extend along the print build direction (Z−direction). The α' phase basically grew along the β phase grain boundaries, forming dense acicle-like martensite structures along the internal boundaries. Obvious acicular martensite microstructure characteristics was shown in Fig. 5(c), which was also consistent with the results of the previous XRD phase characterization.

The morphology of the surface layer of the LRed-Ti6Al4V was presented in Fig. 6. After LR, the pores in the surface layer of the material were significantly reduced, showing obvious micro-structure partitioning phenomenon along the Z direction. Various microstructural characteristics at different depths within the LRed-Ti6Al4V were

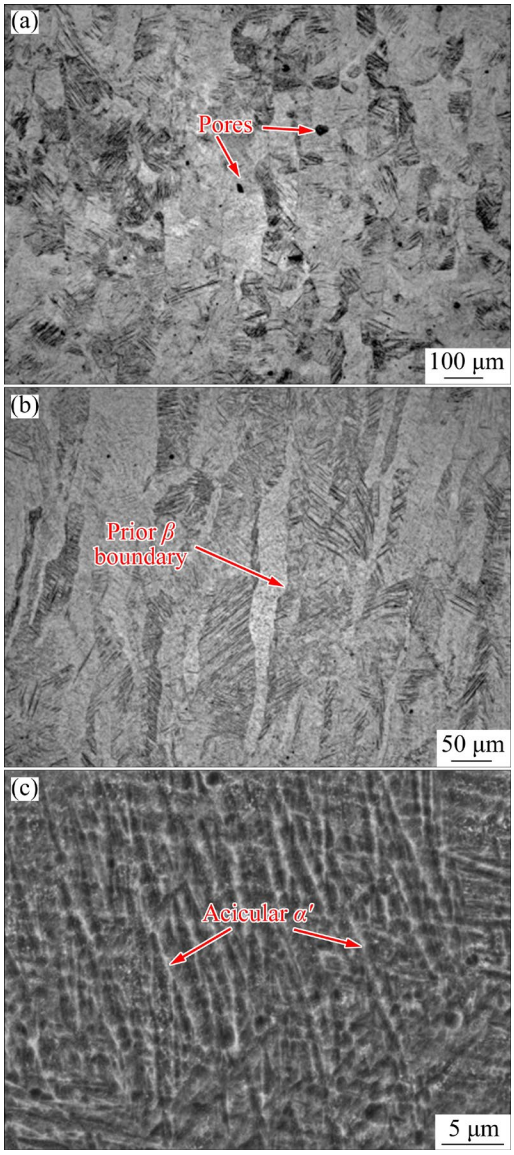

Fig. 5 Morphology of *YOZ* surface of LPBF-Ti6Al4V alloys

revealed in Fig. 6(a), including the melted zone (MZ) and heat-affected zone (HAZ). The depth of the MZ was about 60−70 μm, and the depth of the HAZ was about 80−90 μm.

3.1.3 Effect of LR on orientation distribution

The EBSD analysis was conducted on the cross section of the surface layer of the LPBF-Ti6Al4V sample, as well as on both the MZ and HAZ of the LRed-Ti6Al4V sample. The results of band contrast (BC), grain boundaries (GB) and grain size statistics for each zone are presented in Figs. 7−10.

In Fig. 7, the LPBF-Ti6Al4V sample exhibited notable acicular grain characteristics. Some regions of the sample displayed lath-shaped grains, which

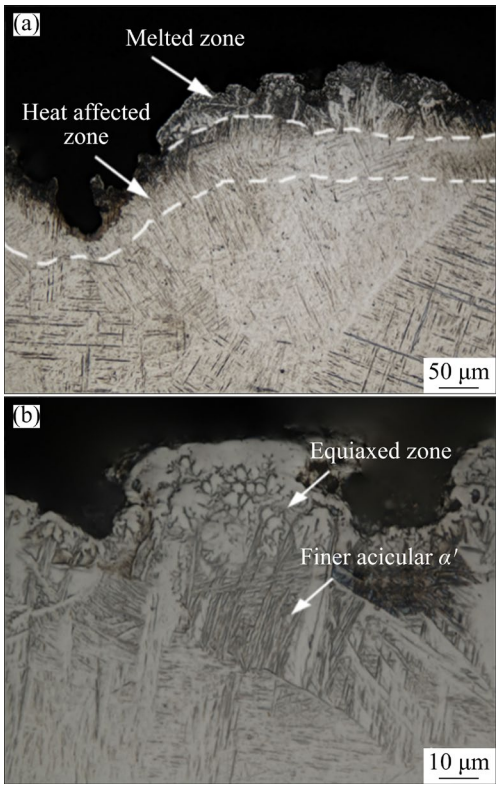

Fig. 6 Morphology of *YOZ* surface of LRed-Ti6Al4V alloys

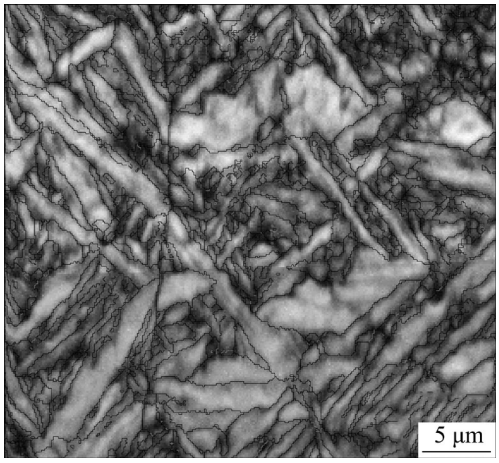

Fig. 7 BC+GB morphology within selected area of cross section of surface layer of LPBF-Ti6Al4V sample

were relatively large in size and had a lower aspect ratio. Overall, the grain size within the LPBF-Ti6Al4V sample was not uniform, with some grains being significantly coarse. The dimensions of the long and short axes of the needle-like α'-Ti grains within the selected area of the LPBF-Ti6Al4V sample were statistically analyzed by Oim-A software, and the results were shown in Figs. 8(a, b), respectively. The size of the long axis of martensite in LPBF-Ti6Al4V ranged from 0.92 to 21.11 μm,

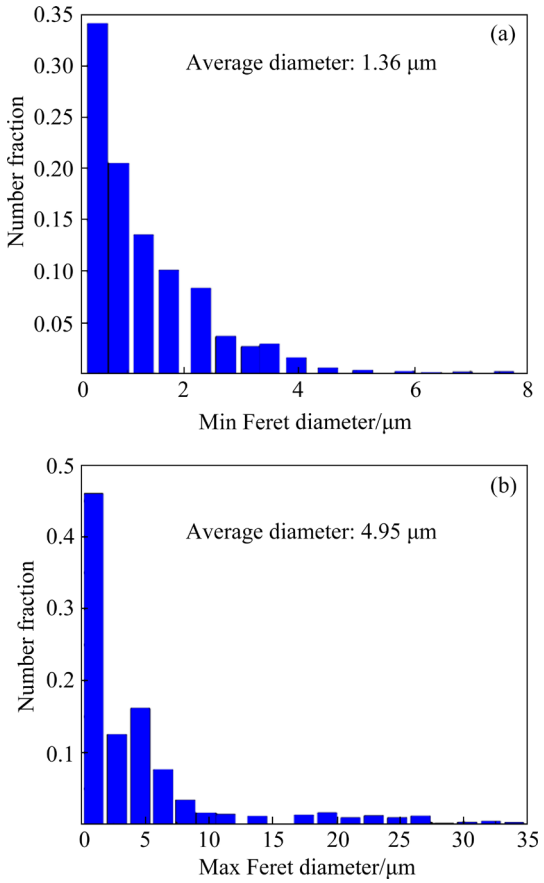

Fig. 8 (a) Short axis sizes within selected zone of LPBF-Ti6Al4V sample; (b) Long axis sizes within selected zone of LPBF-Ti6Al4V sample

with an average of 4.95 μm. The size of the short axis ranged from 0.47 to 7.58 μm, with an average of 1.36 μm.

The BC morphologies of MZ and HAZ of the LRed-Ti6Al4V sample were shown in Fig. 9(a, b), respectively. A uniform, dense, and fine equiaxed grain structure was exhibited in the MZ of the LRed-Ti6Al4V sample. The HAZ of the LRed-Ti6Al4V sample featured significantly at refined acicular α'-Ti grains compared to the LPBF-Ti6Al4V sample. Furthermore, the grain size in the HAZ of the LRed-Ti6Al4V sample was more uniform, and there was no apparent occurrence of coarse grains. As there were equiaxed grains in the MZ of the LRed-Ti6Al4V, OimA software was used to weight the area of each grain in the scanning region and the average value was calculated. The formula was as follows:

$$\overline{d} = \sum_{i=1}^{N} A_i d_i \Big/ \sum_{i=1}^{N} A_i \tag{3}$$

where N is the total number of grains, d_i is the value

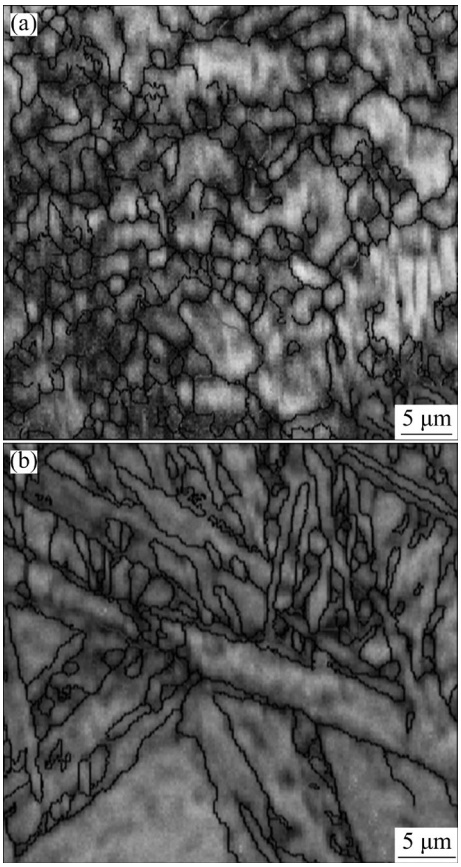

Fig. 9 EBSD images of cross section of (a) MZ and (b) HAZ of LRed-Ti6Al4V sample

of the *i*th grain, and A_i indicates the area of the *i*th grain.

The grain size of the equiaxed grains was shown in Fig. 10(a) with an average size of 1.31 μm. The dimensions of the long and short axes of the α'-Ti grains within the HAZ of the LRed-Ti6Al4V sample were also statistically analyzed by Oim-A software, and the results were shown in Figs. 10(b, c), respectively. The size of the long axis of the martensite in the HAZ of the LRed-Ti6Al4V ranged from 0.82 to 11.67 μm, with an average of 1.98 μm. The size of the short axis ranged from 0.21 to 4.7 μm, with an average of 0.94 μm.

As seen in Fig. 11, the LPBF-Ti6Al4V had the highest texture level (maximum texture intensity of 13.86), while the maximum texture intensities of the MZ and the HAZ of the LRed-Ti6Al4V were 10.79 and 6.35, respectively. It was proven that LR treatment significantly reduced the texture level of the LPBF-Ti6Al4V.

The organizational structures constructed from LPBF and LRed processes would be analyzed in relation to their distinctive process characteristics.

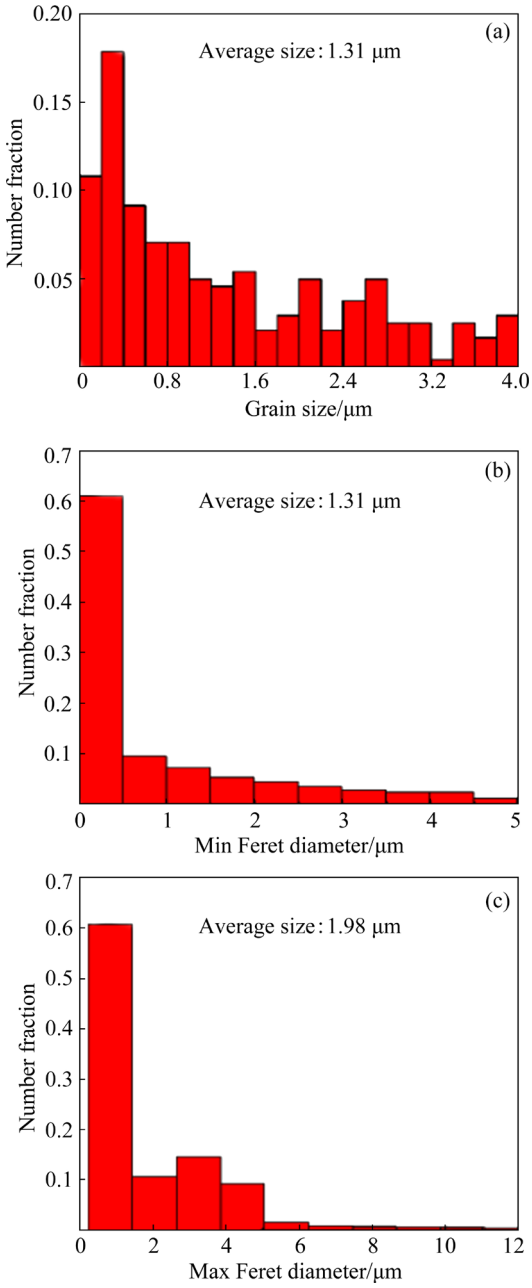

Fig. 10 (a) Grain sizes in MZ of LRed-Ti6Al4V; (b) Short axis sizes within HAZ; (c) Long axis sizes within HAZ

The LPBF treatment employed a multi-pass scanning approach (refer to Fig. 12(a)). After each layer was fused, the printed part underwent a counterclockwise rotation of 67°. Subsequently, the powder fusion of the next layer was carried out. However, as could be seen in Figs. 12(b, d), the LR treatment only completed a single scan of the sample surface, and the stacked overlap of the melt pool happened during the reciprocal scanning process as the fixed laser beam overlap rate was 50%.

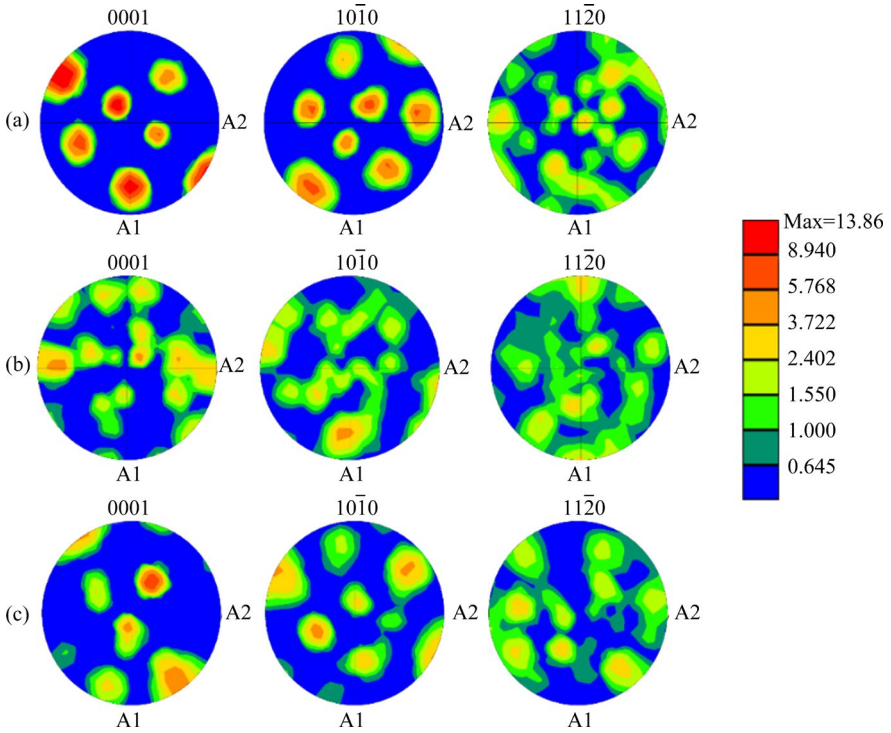

Fig. 11 Characterization of orientation distribution of α' grains within titanium alloys: (a) LPBF; (b) MZ; (c) HAZ (The scale bar represented the values of the texture intensity)

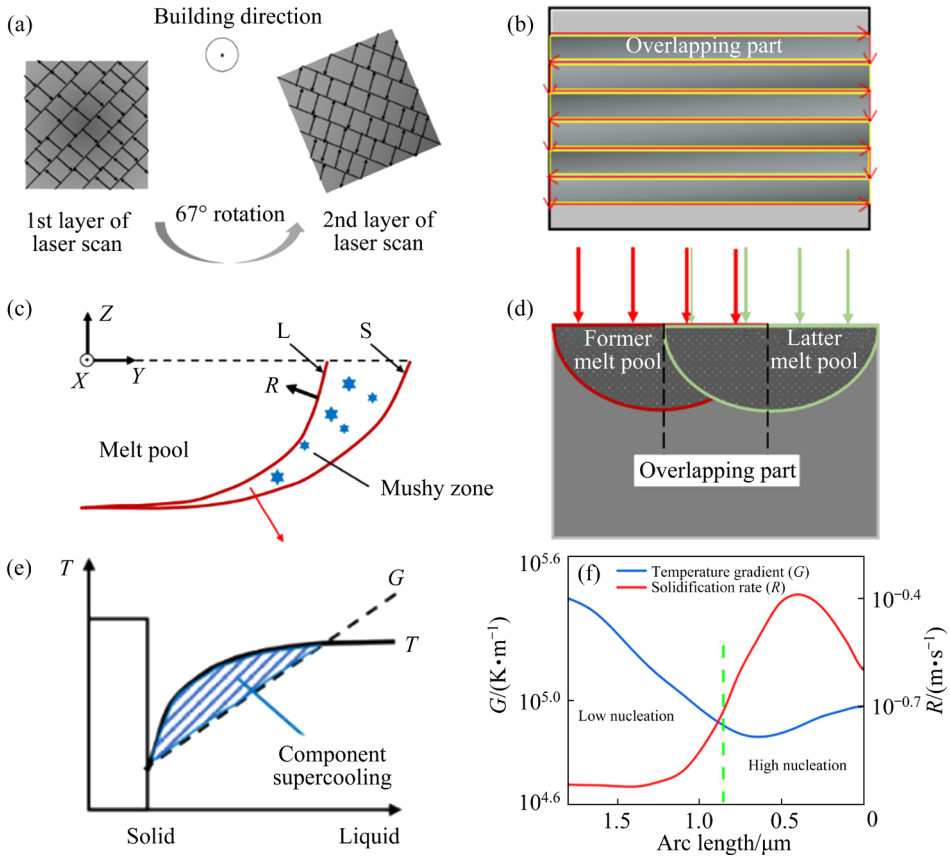

Fig. 12 Mechanism of grain growth in melt pool: (a, b) Schematic scans of LPBF and LR processes, respectively; (c) Schematic of grain nucleation and growth in vicinity of melt pool; (d) Surface melt pool stacking for LR process; (e) Subcooling of components in melt pool; (f) Relationships between G and R and nucleation rate

Upon analyzing the single-pass melt pool, both LPBF and LR processes had extremely high cooling rates (above 10^4 K/s) [36], and there was compositional subcooling during the solidification of the liquid metal, as shown in Figs. 12(c, e). The compositional subcooling zone in Fig. 12(e) was the zone between the temperature gradient and the liquid metal temperature profile. The analysis of the grain growth in the subcooling zone was done in conjunction with the temperature gradient (G) and solidification rate (R) [37]. Previous calculations demonstrated that the laser energy density in the LPBF process surpassed that of the LR process, resulting in a more pronounced heat concentration which led to a larger temperature gradient within the melt pool [38]. Moreover, due to the generally higher thermal conductivity of bulk solid materials compared to powder materials [39], the heat dissipation in the melt pool formed by LPBF process was slower and more inhomogeneous compared to the melt pool of LR, resulting in a slower R and a higher G/R ratio. G and R had a major impact on grain growth during the solidification process of the melt pool, as illustrated in Fig. 12(f) [39]. The LPBF process was characterized by a higher G/R value, smaller supercooling degree, and a lower nucleation rate. Furthermore, grains exhibited a tendency to grow along the maximum thermal gradient, and those with identical orientations displayed a synergistic effect during their growth [22]. Consequently, these factors collectively contributed to an increase in the anisotropy of the internal structure of the LPBF sample. At the top of the LR molten pool, a smaller G/R ratio signified an elevated heterogeneous nucleation rate. As a result, grain growth was no longer predominantly influenced by epitaxial growth. Instead, it tended to initiate nucleation and developed into equiaxed grains [40]. Furthermore, as could be seen in Fig. 12(d), this double scanning procedure reduced texture intensity considerably, which also helped generate fine equiaxial grains in the MZ of the LRed-Ti6Al4V.

A large volume of metal vapors were produced during the melting of the powder under high-energy focusing and migrated into the melt pool since the LPBF process required a higher laser scanning rate. The extremely high cooling rate resulted in a reduction in volatility and the metal vapors could not diffuse out before the completion of single-pass molding, remaining as bubbles inside the specimen and creating pore defects [41,42]. In contrast, during the LR process, remelting−solidification molding occurred on the alloy surface. This process provided sufficient time for heat exchange with the surrounding powder, particularly at a lower scanning speed. As a result, hole defects in the new melt pool were better filled, leading to enhanced sample densification [43].

3.2 Effect of laser remelting on properties of LPBF-Ti6Al4V

3.2.1 Effect of laser remelting on microhardness

The Vickers microhardness tester was utilized to evaluate the microhardness of the LPBF and LRed alloys, and the corresponding microhardness curves were subsequently plotted and presented (Fig. 13). The microhardness values of the surface of the LPBF and LRed samples were $HV_{0.2}$ 323.1 and $HV_{0.2}$ 486.2, respectively. The hardness values of the LPBF-Ti6Al4V showed minimal variation across different depths. In contrast, the hardness of the LRed-Ti6Al4V exhibited a gradual decrease as the depth increased. At the depth of 200 μm, the hardness of the LRed-Ti6Al4V dropped to a value comparable to that of the LPBF-Ti6Al4V. The changes in the microhardness curves of the samples indicated that the effect of LR on the microhardness of LPBF-Ti6Al4V alloy was in the range of about 0−200 μm, as its strengthening effect gradually decreased with increasing depth.

Both LPBF and LRed alloys were mainly composed of α' phase, but grain size was changed significantly. According to the Hall−Petch formula, the grain refinement could cause an increase in the

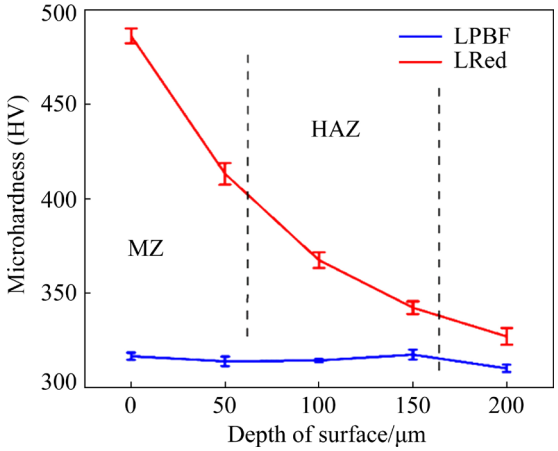

Fig. 13 Microhardness of LPBF-Ti6Al4V and LRed-Ti6Al4V titanium alloys

microhardness of the alloys. In this experiment, fine grain refinement emerged as the primary factor influencing the microhardness. Specifically, a reduction in grain size led to an increase in the number of grain boundaries. The grain boundaries, in turn, acted as obstacles, hindering the movement of internal dislocations. After the treatment of LR, the grains of the surface layer of the sample were refined within the depth range of 0−200 μm. It was consistent with the depth at which the enhancement in microhardness was observed. Furthermore, the treatment of LR could facilitate the reduction of pores in the surface layer of the alloy, thereby mitigating the softening effect caused by pores in the LPBF-Ti6Al4V alloys [44].

3.2.2 Effect of laser remelting on friction and wear properties

The friction coefficients of the LPBF and LRed alloys were shown in Fig. 14(a). At the initial stage of friction, the roughness of the counter-abrasive surface and the friction between the counter-abrasive surface and the sample were small, resulting in a low friction coefficient [45]. The roughness of the ground surface gradually increased with continuous wear, leading to an increase in both friction force and friction coefficient. Moreover, a greater increase was observed in the LPBF-Ti6Al4V. After the transformation period of the pre-grinding, the roughness of the opposing grinding surface tended to stabilize, indicating a shift into a stable wear stage.

The LRed-Ti6Al4V represented a lower average friction coefficient, approximately 0.43, while the LPBF-Ti6Al4V demonstrated a higher average friction coefficient, around 0.48. There was a negative correlation between the microhardness and the amount of sliding friction loss, with higher strength alloys having correspondingly lower friction mass loss during sliding [46]. As presented in Fig. 14(b), the mass loss rate of LPBF-Ti6Al4V alloys was 6.19×10^{-4}, which was higher than that of the LR alloys (4.28×10^{-4}). Figure 15 showed the surface morphology of the samples following wear. The worn surface of the LPBF-Ti6Al4V sample mainly consisted of a large number of parallel deep furrows, with heavy adhesions of wear debris at the edge of the groove. In addition, there were peeling microcracks and local friction balls on the surface, indicating that the sample surface was seriously deformed during the sliding process. Instead, the worn surface of the LRed-Ti6Al4V alloys was much flatter, with shallower wear marks and fewer delaminations, which proved that the wear process of the LRed-Ti6Al4V alloys was more stable.

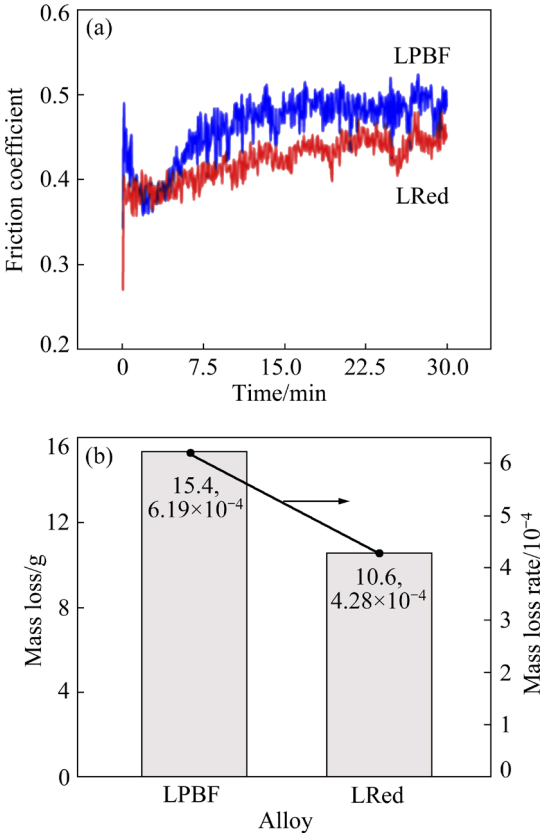

Fig. 14 (a) Friction coefficient and (b) mass loss (rate) of LPBF-Ti6Al4V and LRed-Ti6Al4V alloys

The forces during friction for both samples were discussed (Fig. 16). During the initial stage of friction in the sliding process, the combined effects of the normal load (F_n) and the frictional shear force (F_t) were experienced by the titanium alloy. The surface of the workpiece came into contact with micro-convex bodies of the counter wear material, resulting in elastic deformation of the base material. It was important to note that no abrasive chips or material detachment occurred during the sliding friction process.

As the friction and wear process continued, furrows and abrasive chips were gradually formed, due to the shear action exceeding the critical bearing range of the metal. Consequently, the friction surface underwent plastic deformation [47]. A preferred orientation was exhibited in the LPBF-Ti6Al4V, where the surface grains displayed

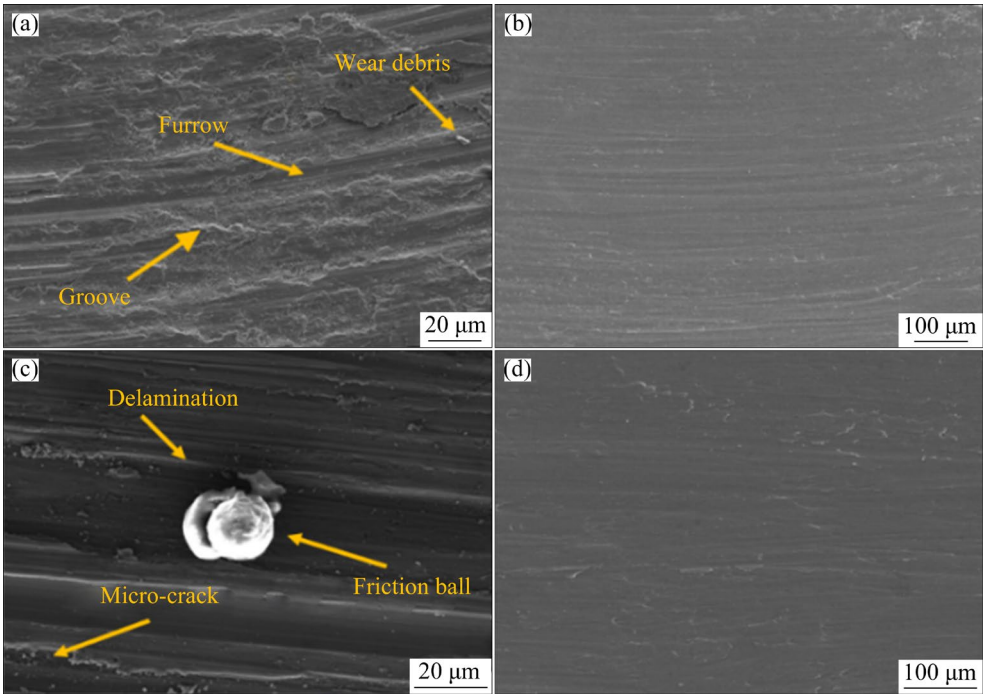

Fig. 15 Surface morphologies after wear: (a, b) LPBF-Ti6Al4V alloys; (c, d) LRed-Ti6Al4V alloys

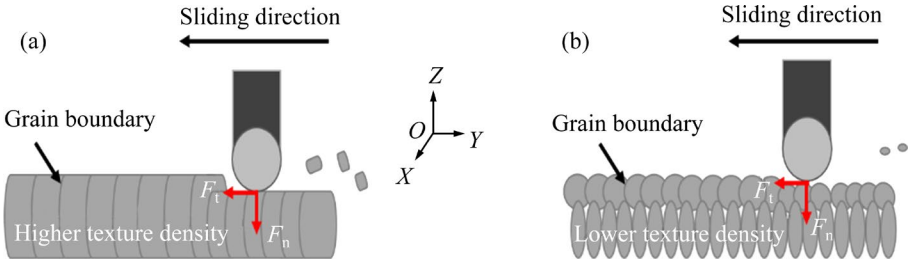

Fig. 16 Force state of (a) LPBF-Ti6Al4V and (b) LRed-Ti6Al4V alloys under friction conditions

epitaxial growth along the *Z* direction, resulting in a significant impact from the cutting and grinding process, which increased the chances of detachment for grains growing along the *Z* direction and led to elevated friction debris [48]. Moreover, it induced new friction pairs on the surface which would lead to severe increased friction losses. The texture intensity of the titanium alloys experienced a remarkable decrease after the LR process and effectively mitigated mass loss.

During the sliding friction process, the LPBF sample and the LRed alloys possessed different wear mechanisms. With high cooling rate and *G*/*R* ratio, there were strong preferred orientation and many pore defects in the LPBF-Ti6Al4V, which led to low microhardness and removal of larger particles [49]. The debris generated during the friction of the LPBF-Ti6Al4V sample remained at the interface between the friction pair and the alloy, resulting in a transformation from two-body wear to three-body wear which generated grooves [50]. The furrows, shear delaminations, and dispersed wear debris were accompanied by thermal changes during dry friction, affecting the surface layer through abrasive wear [51]. After the LR process, the surface grain of the titanium alloy was significantly refined and the gap holes were filled, which effectively addressed the issue of high preferred orientation in the LPBF-Ti6Al4V sample and increased the microhardness. Consequently, the material became less susceptible to tearing during sliding and friction [52]. Instead, adhesive wear became the preferred mode of wear. This shift effectively reduced the mass loss and led to a comprehensive improvement in the friction and wear resistance of the LRed-Ti6Al4V sample.

3.2.3 Influence of laser remelting on electrochemical performance

The polarization curves of the samples were shown in Fig. 17(a), where it could be observed that both samples exhibited the same passivation characteristics in the stable passive state. The Tafel method was utilized to fit the polarization curve, resulting in J_{corr} and φ_{corr} values of 1.88×10^{-8} A/cm^2 and 84.13 mV for the LRed-Ti6Al4V alloys, respetively. In contrast, the LPBF sample exhibited values of 3.16×10^{-7} A/cm^2 and −177.5 mV for J_{corr} and φ_{corr}. Furthermore, both samples displayed distinct capacitor arc characteristics in their Nyquist curves (as shown in Fig. 17(b)), with the LRed-Ti6Al4V sample exhibiting a larger arc radius, indicating its superior corrosion resistance.

The Ti6Al4V alloy underwent electrochemical dissolution in the 3.5 wt.% NaCl solution, forming the TiO_2 oxide layer on its surface [53], which effectively mitigated the erosive impact of Cl^- on the surface of the Ti6Al4V alloy. Furthermore, this oxide layer acted as a passivation film that safeguarded the internal matrix:

$$Ti \rightarrow Ti^{4+}+4e \quad (4)$$

$$Ti^{4+}+2H_2O \rightarrow TiO_2+4H^+ \quad (5)$$

An equivalent circuit model was established for the two samples (Fig. 17(c)). The equivalent circuit consisted of a parallel combination of a resistor and a capacitor (RC). R_s, R_f, R_t, and CPE represented solution resistance, passivated zone resistance, internal charge transfer resistance, and the constant phase element, respectively. CPE-T referred to a double-layer capacitor. The ZView software was used to perform fitting analysis on the EIS data of the samples, which yielded the parameters presented in Table 3.

It could be observed from Table 3 that the values of R_s, R_f, and R_t for the LRed-Ti6Al4V alloys showed considerable increases compared to the LPBF-Ti6Al4V, particularly in terms of R_t, indicating that the passivation film of LRed-Ti6Al4V provided stronger protection. From the perspective of corrosion thermodynamics, the self-corrosion potential (φ_{corr}) of the LRed-Ti6Al4V moved in the positive direction, indicating a lower

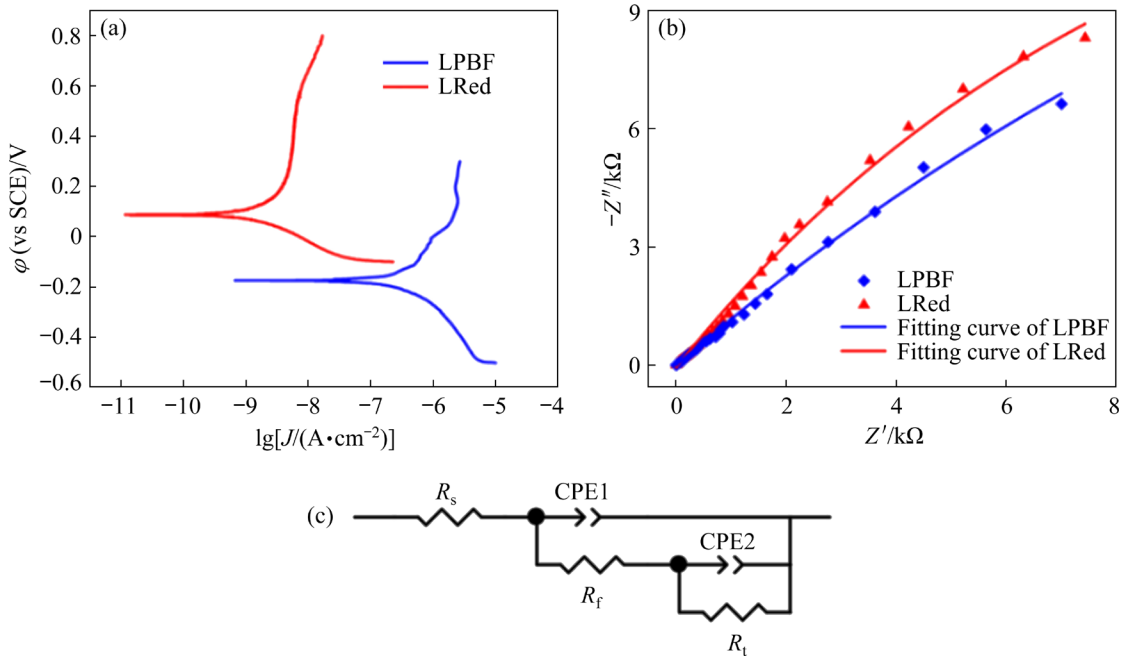

Fig. 17 Characterization of electrochemical properties of LPBF-Ti6Al4V and LRed-Ti6Al4V alloys: (a) Polarization curve plot; (b) Impedance; (c) Equivalent circuit diagram

Table 3 EIS fitting results of LPBF-Ti6Al4V and LRed-Ti6Al4V samples

Sample	R_s/ ($\Omega\cdot$cm^2)	CPE1-T/ ($10^{-6}\ \Omega^{-1}\cdot$cm$^{-1}\cdot$s^n)	R_f/ ($\Omega\cdot$cm^2)	CPE2-T/ ($10^{-6}\cdot\Omega^{-1}\cdot$cm$^{-1}\cdot$s^n)	R_t/ ($\Omega\cdot$cm^2)
LPBF	3.20	128.33	687	2312	7247
LRed	18.8	68.82	924	1263	20201

tendency for electrochemical corrosion. From the perspective of corrosion kinetics, J_{corr} of the LRed-Ti6Al4V was reduced and its surface polarization resistance and electrochemical impedance were increased after LR, indicating a lower corrosion rate and enhanced corrosion resistance [54].

The surface morphologies of the samples following corrosion treatment were shown in Fig. 18. Upon comparing the surface morphology (Figs. 18(a, c)), it was evident that significant pitting holes were formed on the LPBF-Ti6Al4V, with relatively deep corrosion depths observed within these pits. Additionally, there were micro-cracks at the edges of these pits, along with shedding particles. Conversely, a flatter surface without any prominent pitting holes was observed in the LRed-Ti6Al4V (Fig. 18(c)), demonstrating that LR treatment could enhance the corrosion resistance of materials. Besides, Cl^- ions could induce pitting on metal and alloy surfaces, as proposed by MACDONALD [55], who suggested that the critical corrosion potential of materials was a linear function of logarithm of Cl^- content. ROLSTEN [56] further proposed that the dissolution of Ti element was governed by formation of $TiCl_4$ complexes:

$$Ti+4Cl^- \rightarrow TiCl_4+4e \quad (6)$$

$$TiCl_4+2H_2O \rightarrow TiO_2+4Cl^-+4H^+ \quad (7)$$

Within the range of polarization potential, Cl^- ions in the corrosive environment penetrated through the passivation film and infiltrated into the interior of the metal, resulting in the occurrence of localized pitting corrosion and the exposure of the underlying substrate [57]. This led to the formation of an active−passive galvanic cell consisting of the internal substrate and the surface passivation film. The anode (internal substrate), which occupied a smaller area, corroded to a deeper depth, increasing the pitting degree [58]. Both samples, as depicted in Figs. 18(b, d), were subjected to element surface scanning. The scanning result revealed an absence of Ti element and a preponderance of Al and O elements at the sites of the holes on the corroded surface.

As seen in Tables 4 and 5, the surface Al content of LRed-Ti6Al4V alloys after corrosion was significantly lower than that of LPBF samples, and the selection sites 1 and 2 on the surface of the samples were mainly Al_2O_3, indicating that the TiO_2 passivation film on the corroded surface of the LRed-Ti6Al4V alloys was more complete and could be more effective in protecting the internal matrix. Al_2O_3 was developed in the internal matrix when Cl^- broke through and damaged the surface protective layer, and hence, the amount of Al element on the corrosion surface could also be used as a reference to evaluate the corrosion resistance of the TiO_2 passivation film [59].

The electrochemical corrosion resistance of the LPBF-Ti6Al4V alloy was significantly enhanced after undergoing LR treatment. Equiaxed grains

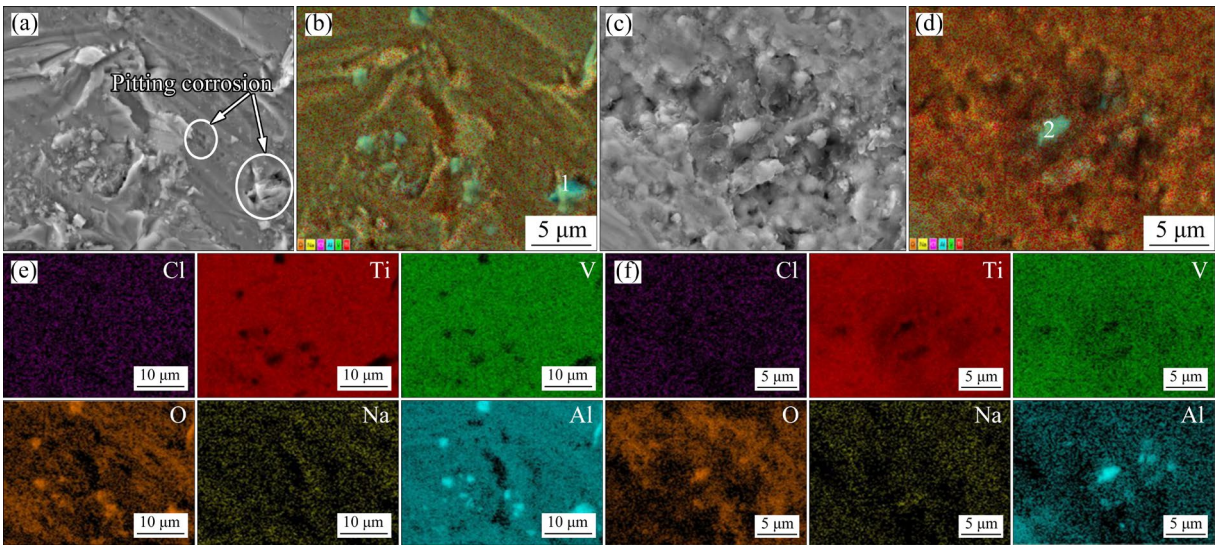

Fig. 18 SEM images of corrosion surface of titanium alloys: (a, c) Microscopic morphologies of LPBF and LRed alloys, respectively; (b, e) Distribution of elements within selected area of LPBF alloys; (d, f) Distribution of elements within selected area of LRed alloys

Table 4 Element content of two samples (at.%)

Sample	Ti	O	Al	V	Na, Cl
LPBF	51.40	39.26	7.02	2.23	Bal.
LRed	43.61	54.23	1.13	0.76	Bal.

Table 5 Elemental content of selected sites in Fig. 18 of two samples (at.%)

Site	O	Al	Ti	V	Na, Cl
1	60.54	37.70	1.41	0.17	Bal.
2	56.39	30.16	5.12	0.34	Bal.

showed better corrosion resistance than acicular grains of the same size, even though they had the same phase composition, according to earlier research [60]. At the top of melt pool of the LRed-Ti6Al4V, the microstructure of the MZ changed from massive acicular grains to finer, more uniform equiaxed grains, while the acicular grains in the HAZ underwent a notable refinement. There were larger grain boundaries on the surface of the LRed-Ti6Al4V alloys, providing more nucleation sites for the formation of the passivation film [61,62]. This strengthened the adhesion of the film to the surface and promoted the formation of a denser protective coating, decreasing the sensitivity of pitting [63]. Furthermore, the LR treatment effectively eliminated the remaining voids in the LPBF sample, improving the density of the material surface and partially prevented Cl^- ions from further penetrating into the passivation film [64].

4 Conclusions

(1) The grains in MZ were presented as fine equiaxed grains with an average size of 1.31 μm, and the acicle-like grains were refined to 0.82−11.67 and 0.12−4.7 μm in the HAZ. The holes in the surface were filled after LR and the density of the alloys was significantly increased due to the lower scanning rate during LR. Moreover, the texture intensity decreased in MZ and HAZ. The transformation could be attributed to a smaller G/R ratio and higher heterogeneous nucleation rate in the remelt pool, as well as two competing mechanisms: epitaxial growth and equiaxed crystal formation.

(2) The surface microhardness increased, the average friction coefficient decreased, and the mass loss rate reduced after LR. The combined effects of density improvement and grain refinement resulted in the increased microhardness of LRed-Ti6Al4V. Furthermore, the LRed-Ti6Al4V showed less susceptibility to chip removal and wear off due to its finer structure and lower anisotropy, which lowered the likelihood of abrasive wear and ultimately enhanced overall wear resistance.

(3) The improved density and refined grains resulted in the formation of a tighter passivation film, which significantly enhanced the electrochemical corrosion resistance after LR.

CRediT authorship contribution statement

Yue-yang LIU: Investigation, Data curation, Visualization, Writing − Original draft, Formal analysis; **Yang YANG:** Project administration, Funding acquisition, Conceptualization, Supervision, Validation, Writing − Review & editing; **Xiang CHEN:** Validation; **Yu-xing ZHAN:** Investigation, Data curation, Visualization, Writing − Original draft, Formal analysis.

Declaration of competing interest

The authors declare that they have no known competing financial interests or personal relationships that could have appeared to influence the work reported in this paper.

Data and code availability

The data underlying this article cannot be shared publicly for the privacy of individuals that participated in the study.

Acknowledgments

This work was supported by the National Natural Science Foundation of China (No. 51871243), the National Key Laboratory of Strength and Structural Integrity, China (No. ASSIKFJJ202304001), the State Key Laboratory of Precision Blasting and Hubei Key Laboratory of Blasting Engineering, China (No. PBSKL2022C01), the Guangdong−Hong Kong−Macao Joint Laboratory for Neutron Scattering Science and Technology, China (No. HT-CSNS-DG-CD-0092/2021), the Shock and Vibration of Engineering Materials and Structures Key Laboratory of Sichuan Province, China (No. 22kfgk06), and the Hubei Longzhong Laboratory, China (No. 2022KF-08).

References

[1] GONG Hai-jun, RAFI K, GU Heng-feng, STARR T, STUCKER B. Analysis of defect generation in Ti−6Al−4V parts made using powder bed fusion additive manufacturing

processes [J]. Additive Manufacturing, 2014, 1/2/3/4: 87−98. DOI: https://doi.org/10.1016/j.addma.2014.08.002.

[2] YANG Yu-xi, GAO Wei-hong, SUN Bin, FU Yu-dong, MENG Xiang-long. Recent advances on additive manufactured shape memory alloys [J]. Transactions of Nonferrous Metals Society of China, 2024, 34(7): 2045−2073. DOI: https://doi.org/10.1016/S1003-6326(24)66525-8.

[3] SUN Yi, YI Zhong-huai, SHEN Ting, XIONG Hui-wen, KANG Xiao, ZHANG Lei, ZHOU Ke-chao. Microstructure and mechanical properties of 7075 aluminum alloy prepared by metal fused deposition modeling [J]. Transactions of Nonferrous Metals Society of China, 2024, 34(7): 2108−2119. DOI: https://doi.org/10.1016/S1003-6326(24)66528-3.

[4] LIU Yue-yang, YANG Yang, CHEN Chao. Microstructure and properties of Ni−Ti based gradient laser cladding layer of Ti6Al4V alloy by laser powder bed fusion [J]. Additive Manufacturing, 2024, 79: 103906. DOI: https://doi.org/10.1016/j.addma.2023.103906.

[5] WANG Pei, LAO Chang-shi, CHEN Zhang-wei, LIU Ying-kuo, WANG Hao, WENDROCK H, ECKERT J, SCUDINO S. Microstructure and mechanical properties of Al−12Si and Al−3.5Cu−1.5Mg−1Si bimetal fabricated by selective laser melting [J]. Journal of Materials Science and Technology, 2020, 36: 18−26. DOI: https://doi.org/10.1016/j.jmst.2019.03.047.

[6] LIU Zheng, ZHANG Lian-min, REN De-chun, MA Ai-li, JI Hai-bin, ZHENG Yu-gui. Corrosion behavior of Ti−6Al−4V alloy fabricated by selective laser melting in simulated spent fuel reprocessing environment [J]. Transactions of Nonferrous Metals Society of China, 2024, 34(7): 2167−2180. DOI: https://doi.org/10.1016/S1003-6326(24)66532-5.

[7] QIU Yi, LI Ying-ju, FENG Xiao-hui, ZHANG Ang, YANG Yuan-sheng. Numerical simulation of microstructure evolution in molten pool of nickel-based superalloy during selective laser melting [J]. Transactions of Nonferrous Metals Society of China, 2024, 34(2): 560−575. DOI: https://doi.org/10.1016/S1003-6326(23)66417-9.

[8] BANERJEE D, WILLIAMS J C. Perspectives on titanium science and technology [J]. Acta Materialia, 2013, 61(3): 844−879. DOI: https://doi.org/10.1016/j.actamat.2012.10.043.

[9] LIU Shi-shuang, CAI Jian-ming, ZHOU Yi, CAO Jing-xia, ZHANG Wang-feng, DAI Sheng-long, HUANG Xu, CAO Chun-xiao. Influence of annealing temperature on microstructural evolution and tensile behavior of Ti−6Al−4V alloy manufactured by multi-directional forging [J]. Transactions of Nonferrous Metals Society of China, 2024, 34(6): 1864−1877. DOI: https://doi.org/10.1016/S1003-6326(24)66512-X.

[10] HEINL P, MÜLLER L, KÖRNER C, SINGER R F, MÜLLER F A. Cellular Ti−6Al−4V structures with interconnected macro porosity for bone implants fabricated by selective electron beam melting [J]. Acta Biomaterialia, 2008, 4(5): 1536−1544. DOI: https://doi.org/10.1016/j.actbio.2008.03.013.

[11] WANG Jin-cheng, ZHU Rui, LIU Yu-jing, ZHANG Lai-chang. Understanding melt pool characteristics in laser powder bed fusion: An overview of single- and multi-track melt pools for process optimization [J]. Advanced Powder Materials, 2023, 2(4): 100137. DOI: https://doi.org/10.1016/j.apmate.2023.100137.

[12] MERCELIS P, KRUTH P J. Residual stresses in selective laser sintering and selective laser melting [J]. Rapid Prototyping Journal, 2006, 12: 254−265. DOI: https://doi.org/10.1108/13552540610707013.

[13] CHEN Xin-yue, XIE Xin-liang, WU Hao, JI Xia, SHEN Hao-peng, XUE Mu-han, WU He, CHAO Qi, FAN Guo-hua, LIU Qing. In-situ control of residual stress and its distribution in a titanium alloy additively manufactured by laser powder bed fusion [J]. Materials Characterization, 2023, 201: 112953. DOI: https://doi.org/10.1016/j.matchar.2023.112953.

[14] KUAI Ze-zhou, LI Zhong-hua, LIU Bin, LIU Wen-peng, YANG Shuai. Effects of remelting on the surface morphology, microstructure and mechanical properties of AlSi10Mg alloy fabricated by selective laser melting [J]. Materials Chemistry and Physics, 2022, 285: 125901. DOI: https://doi.org/10.1016/j.matchemphys.2022.125901.

[15] JIAO Ze-hui, WU Xue-ren, YU Hui-chen, XU Rui-da, WU Ling-liang. High cycle fatigue behavior of a selective laser melted Ti6Al4V alloy: Anisotropy, defects effect and life prediction [J]. International Journal of Fatigue, 2023, 167: 107252. DOI: https://doi.org/10.1016/j.ijfatigue.2022.107252.

[16] LI Cheng-lin, HONG J K, NARAYANA P L, CHOI S W, LEE S W, PARK C H, YEOM J T, MEI Qing-song. Realizing superior ductility of selective laser melted Ti−6Al−4V through a multi-step heat treatment [J]. Materials Science and Engineering A, 2021, 799: 140367. DOI: https://doi.org/10.1016/j.msea.2020.140367.

[17] BUCHBINDER D, MEINERS W, PIRCH N, WISSENBACH K, SCHRAGE J. Investigation on reducing distortion by preheating during manufacture of aluminum components using selective laser melting [J]. Journal of Laser Applications, 2013, 26(1): 012004. DOI: https://doi.org/10.2351/1.4828755.

[18] ZHANG Xiang, MARTINA F, DING J, WANG X, WILLIAMS S W. Fracture toughness and fatigue crack growth rate properties in wire + arc additive manufactured Ti−6Al−4V [J]. Fatigue & Fracture of Engineering Materials & Structures, 2017, 40(5): 790−803. DOI: https://doi.org/10.1111/ffe.12547.

[19] YAN Xing-chen, LUPOI R, WU Hong-jian, MA Wen-you, LIU Min, O'DONNELL G, YIN Shuo. Effect of hot isostatic pressing (HIP) treatment on the compressive properties of Ti6Al4V lattice structure fabricated by selective laser melting [J]. Materials Letters, 2019, 255: 126537. DOI: https://doi.org/10.1016/j.matlet.2019.126537.

[20] COLEGROVE P A, COULES H E, FAIRMAN J, MARTINA F, KASHOOB T, MAMASH H, COZZOLINO L D. Microstructure and residual stress improvement in wire and arc additively manufactured parts through high-pressure rolling [J]. Journal of Materials Processing Technology, 2013, 213: 1782−1791. DOI: https://doi.org/10.1016/j.jmatprotec.2013.04.012.

[21] ALMANGOUR B, YANG J M. Improving the surface quality and mechanical properties by shot-peening of 17-4

stainless steel fabricated by additive manufacturing [J]. Materials & Design, 2016, 110: 914−924. DOI: https://doi.org/10.1016/j.matdes.2016.08.037.

[22] HE Bei, SHAO Wen-peng, TIAN Xiang-jun. Surface grain formation mechanism in the laser remelting molten pool of a near-β titanium alloy [J]. Materialia, 2022, 24: 101521. DOI: https://doi.org/10.1016/j.mtla.2022.101521.

[23] KIRKA M M, NANDWANA P, LEE Y, DEHOFF R R. Solidification and solid-state transformation sciences in metals additive manufacturing [J]. Scripta Materialia, 2017, 135: 130−134. DOI: https://doi.org/10.1016/j.scriptamat.2017.01.005.

[24] ZHANG Du-yao, QIU Dong, ZHU Su-ming. DARGUSCH M, STJOHN D, EASTON M. Grain refinement in laser remelted Mg−3Nd−1Gd−0.5Zr alloy [J]. Scripta Materialia, 2020, 183: 12−16. DOI: https://doi.org/10.1016/j.scriptamat.2020.03.006.

[25] MUKHERJEE S, DHARA S, SAHA P. Enhanced corrosion, tribocorrosion resistance and controllable osteogenic potential of stem cells on micro-rippled Ti6Al4V surfaces produced by pulsed laser remelting [J]. Journal of Manufacturing Processes, 2021, 65: 119−133. DOI: https://doi.org/10.1016/j.jmapro.2021.03.023.

[26] LIEN H H, MAZUMDER J, WANG Jian, MISRA A. Microstructure evolution and high density of nanotwinned ultrafine Si in hypereutectic Al−Si alloy by laser surface remelting [J]. Materials Characterization, 2021, 161: 110147. DOI: https://doi.org/10.1016/j.matchar.2020.110147.

[27] THIJS L, VERHAEGHE F, CRAEGHS T, HUMBEECK J V, KRUTH J P. A study of the microstructural evolution during selective laser melting of Ti−6Al−4V [J]. Acta Materialia, 2010, 58(9): 3303−3312. DOI: https://doi.org/10.1016/j.actamat.2010.02.004.

[28] LIU Yue-yang, GAO Shi-you, ZHAO Wei. Laser cladding of Mg−Zn−Y−Zr alloy using Al with different ratios of micro- and nano-SiC powder [J]. Journal of Materials Science, 2020, 55(27): 13270−13293. DOI: https://doi.org/10.1007/s10853-020-04893-z.

[29] COELHO J P, ABREU M A, PIRES M C. High-speed laser welding of plastic films [J]. Optics and Lasers in Engineering, 2000, 34(4): 385−395. DOI: https://doi.org/10.1016/S0143-8166(00)00071-3.

[30] FANG Min-han, HU Fu-guo, HAN Yuan-fei, LE Jian-wen, XI Jiang-jing, SONG Jing-wen, KE Lin-da, XIAO Mei-li, LU Wei-jie. Controllable mechanical anisotropy of selective laser melted Ti6Al4V: A new perspective into the effect of grain orientations and primary grain structure [J]. Materials Science and Engineering A, 2021, 827: 142031. DOI: https://doi.org/10.1016/j.msea.2021.142031.

[31] ZHENG Zhong-peng, JIN Xin, BAI Yu-chao, YANG Yun, NI Chen-bing, LU Wen-feng, WANG Hao. Microstructure and anisotropic mechanical properties of selective laser melted Ti6Al4V alloy under different scanning strategies [J]. Materials Science and Engineering A, 2022, 831: 142236. DOI: https://doi.org/10.1016/j.msea.2021.142236.

[32] LI De-yu, O'CONNOR B H, CHEN Qi-tao, ZADNIK M G. Quantitative powder X-ray diffractometry phase analysis of silicon nitride materials by a multiline, mean-normalized-intensity method [J]. Journal of the American Ceramic Society, 1994, 77(8): 2195−2198. DOI: https://doi.org/10.1111/j.1151-2916.1994.tb07118.x.

[33] LIU Z, WEN X D, WU X L, GAO Y J, CHEN H T, ZHU J, CHU P K. Intrinsic dipole-field-driven mesoscale crystallization of core−shell ZnO mesocrystal microspheres [J]. Journal of the American Chemical Society, 2009, 131(26): 9405−9412. DOI: https://doi.org/10.1021/ja9039136.

[34] LIU Fu-lin, CHEN Yao, LI Lang, WANG Chong, WANG Qing-yuan, LIU Yong-jie. Interior defect-induced crack initiation mechanism and initial growth behavior for Ti6Al4V alloy fabricated using laser powder bed fusion [J]. Journal of Materials Research and Technology, 2022, 21: 2089−2104. DOI: https://doi.org/10.1016/j.jmrt.2022.10.043.

[35] WEI Kai-wen, GAO Ming, WANG Ze-min, ZENG Xiao-yan. Effect of energy input on formability, microstructure and mechanical properties of selective laser melted AZ91D magnesium alloy [J]. Materials Science and Engineering A, 2014, 611: 212−222. DOI: https://doi.org/10.1016/j.msea.2014.05.092.

[36] DILIP J J S, ZHANG Shan-shan, TENG Chong, ZENG Kai, ROBINSON C, PAL D, STUCKER B. Influence of processing parameters on the evolution of melt pool, porosity, and microstructures in Ti−6Al−4V alloy parts fabricated by selective laser melting [J]. Progress in Additive Manufacturing, 2017, 2(3): 157−167. DOI: https://doi.org/10.1007/s40964-017-0030-2.

[37] ZHOU Jian-tao, HAN Xu, LI Hui, LIU Sheng, YI Jun-chao. Investigation of layer-by-layer laser remelting to improve surface quality, microstructure, and mechanical properties of laser powder bed fused AlSi10Mg alloy [J]. Materials & Design, 2021, 210: 110092. DOI: https://doi.org/10.1016/j.matdes.2021.110092.

[38] BONTHA S, KLINGBEIL N W, KOBRYN P A, FRASER H L. Effects of process variables and size-scale on solidification microstructure in beam-based fabrication of bulky 3D structures [J]. Materials Science and Engineering A, 2009, 513/514: 311−318. DOI: https://doi.org/10.1016/j.msea.2009.02.019.

[39] LIU Peng-wei, WANG Zhuo, XIAO Yao-hong, HORSTEMEYER M F, CUI Xiang-yang, CHEN Lei. Insight into the mechanisms of columnar to equiaxed grain transition during metallic additive manufacturing [J]. Additive Manufacturing, 2019, 26: 22−29. DOI: https://doi.org/10.1016/j.addma.2018.12.019.

[40] SONG Jun, TANG Qian, FENG Qi-xiang, HAN Quan-quan, MA Shuai, CHEN Hao, GUO Fu-yu, SETCHI R. Effect of remelting processes on the microstructure and mechanical behaviours of 18Ni-300 maraging steel manufactured by selective laser melting [J]. Materials Characterization, 2022, 184: 111648. DOI: https://doi.org/10.1016/j.matchar.2021.111648.

[41] TANG Xu, ZHANG Song, ZHANG Chun-hua, CHEN Jiang, ZHANG Jing-bo, LIU Yu. Optimization of laser energy density and scanning strategy on the forming quality of 24CrNiMo low alloy steel manufactured by SLM [J]. Materials Characterization, 2020, 170: 110718. DOI: https://doi.org/10.1016/j.matchar.2020.110718.

[42] MARTIN É, AZZI M, SALISHCHEV G A, SZPUNAR J.

Influence of microstructure and texture on the corrosion and tribocorrosion behavior of Ti−6Al−4V [J]. Tribology International, 2010, 43(5): 918−924. DOI: https://doi.org/10.1016/j.triboint.2009.12.055.

[43] XIAO Zhong-xu, CHEN Chang-peng, HU Zhi-heng, ZHU Hai-hong, ZENG Xiao-yan. Effect of rescanning cycles on the characteristics of selective laser melting of Ti6Al4V [J]. Optics & Laser Technology, 2020, 122: 105890. DOI: https://doi.org/10.1016/j.optlastec.2019.105890.

[44] HOSEINI M, SHAHRYARI A, OMANOVIC S, SZPUNAR J A. Comparative effect of grain size and texture on the corrosion behaviour of commercially pure titanium processed by equal channel angular pressing [J]. Corrosion Science, 2009, 51(12): 3064−3067. DOI: https://doi.org/10.1016/j.corsci.2009.08.017.

[45] YUAN Shuo, LIN Nai-ming, ZOU Jian-juan, LIN Xiu-zhou, LIU Zhi-qi, YU Yuan, WANG Zhen-xia, ZENG Qun-feng, CHEN Weng-ang, TIAN Lin-hai, QIN Lin, XIE Rui-zhen, LI Bo-qiong, ZHANG Hong-xia, WANG Zhi-hua, TANG Bin, WU Yu-cheng. In-situ fabrication of gradient titanium oxide ceramic coating on laser surface textured Ti6Al4V alloy with improved mechanical property and wear performance [J]. Vacuum, 2020, 176: 109327. DOI: https://doi.org/10.1016/j.vacuum.2020.109327.

[46] YANG Xin, WANG Wan-lin, MA Wen-jun, WANG Yan, YANG Jun-gang, LIU Shi-feng, TANG Hui-ping. Corrosion and wear properties of micro-arc oxidation treated Ti6Al4V alloy prepared by selective electron beam melting [J]. Transactions of Nonferrous Metals Society of China, 2020, 30(8): 2132−2142. DOI: https://doi.org/10.1016/S1003-6326(20)65366-3.

[47] LIU Heng, HUANG Xin, HUANG Shi-yu, QIAO Li-jie, YAN Yu. Anisotropy of wear and tribocorrosion properties of L-PBF Ti6Al4V [J]. Journal of Materials Research and Technology, 2023, 25: 2690−2701. DOI: https://doi.org/10.1016/j.jmrt.2023.06.128.

[48] LIANG Xiong, DU Ping, LI Shuang-shou, ZHANG Chen-hui. Tribological properties of additive manufactured Ti6Al4V against cemented carbide under dry sliding conditions [J]. Tribology International, 2022, 167: 107358. DOI: https://doi.org/10.1016/j.triboint.2021.107358.

[49] WEI Kai-wen, WANG Ze-min, LI Fang-zhi, ZHANG Hu, ZENG Xiao-yun. Densification behavior, microstructure evolution, and mechanical performances of selective laser melted Ti−5Al−2.5Sn α titanium alloy: Effect of laser energy input [J]. Journal of Alloys and Compounds, 2019, 774: 1024−1035. DOI: https://doi.org/10.1016/j.jallcom.2018.09.153.

[50] YANG Ye, ZHANG Chen-hui, WANG Yan, DAI Yuan-jing, LUO Jian-bin. Friction and wear performance of titanium alloy against tungsten carbide lubricated with phosphate ester [J]. Tribology International, 2016, 95: 27−34. DOI: https://doi.org/10.1016/j.triboint.2015.10.031.

[51] LI X X, ZHOU Y, JI X L, LI Y X, WANG S Q. Effects of sliding velocity on tribo-oxides and wear behavior of Ti−6Al−4V alloy [J]. Tribology International, 2015, 91: 228-234. DOI: https://doi.org/10.1016/j.triboint.2015.02.009.

[52] GU Dong-dong, HAGEDORN Y C, MEINERS W, MENG Guang-bin, BATISTA R J S, WISSENBACH K, POPRAWE R. Densification behavior, microstructure evolution, and wear performance of selective laser melting processed commercially pure titanium [J]. Acta Materialia, 2012, 60: 3849−3860. DOI: https://doi.org/10.1016/j.actamat.2012.04.006.

[53] POHRELYUK I M, FEDIRKO V M, TKACHUK O V, PROSKURNYAK R V. Corrosion resistance of Ti−6Al−4V alloy with nitride coatings in Ringer's solution [J]. Corrosion Science, 2013, 66: 392−398. DOI: https://doi.org/10.1016/j.corsci.2012.10.005.

[54] ZHANG Zhen, WANG Li-qing, ZHANG Rui-ze, YIN De-zheng, ZHAO Zhan-yong, BAI Pei-kang, LIU Bin, WANG Fu-de. Effect of solution annealing on microstructures and corrosion behavior of wire and arc additive manufactured AZ91 magnesium alloy in sodium chloride solution [J]. Journal of Materials Research and Technology, 2022, 18: 416−427. DOI: https://doi.org/10.1016/j.jmrt.2022.02.092.

[55] MACDONALD D D. The history of the point defect model for the passive state: A brief review of film growth aspects [J]. Electrochimica Acta, 2011, 56(4): 1761−1772. DOI: https://doi.org/10.1016/j.electacta.2010.11.005.

[56] ROLSTEN R F. Solution chemistry of the electrochemical machining of titanium, niobium and tantalum [J]. Journal of Applied Chemistry, 1968, 18(10): 292−296. DOI: https://doi.org/10.1002/jctb.5010181002.

[57] RAETZER-SCHEIBE H J. The relationship between repassivation behavior and pitting corrosion for Ti and Ti6Al4V [J]. Corrosion, 1978, 34(12): 437−442. DOI: https://doi.org/10.5006/0010-9312-34.12.437.

[58] SOLTIS J. Passivity breakdown, pit initiation and propagation of pits in metallic materials − Review [J]. Corrosion Science, 2015, 90: 5−22. DOI: https://doi.org/10.1016/j.corsci.2014.10.006.

[59] RALSTON K D, BIRBILIS N. Effect of grain size on corrosion: A review [J]. Corrosion, 2010, 66(7): 7500501−7500513. DOI: https://doi.org/10.5006/1.3462912.

[60] ZUO Han-yang, DENG Hao, ZHOU Lv-jun, QIU Wen-bin, XU Ping, WEI Yong-qiang, PENG Hua-qiao, XIA Zu-xi, TANG Jun. The effect of heat treatment on corrosion behavior of selective laser melted Ti−5Al−5Mo−5V−3Cr−1Zr alloy [J]. Surface and Coatings Technology, 2022, 445(15): 128743. DOI: https://doi.org/10.1016/j.surfcoat.2022.128743.

[61] WANG Li-ping, LIN Yi-min, ZENG Zhi-xiang, LIU Wei-min, XUE Qun-ji, HU Li-tian, ZHANG Jun-yan. Electrochemical corrosion behavior of nanocrystalline Co coatings explained by higher grain boundary density [J]. Electrochimica Acta, 2007, 52(13): 4342−4350. DOI: https://doi.org/10.1016/j.electacta.2006.12.009.

[62] KIM H S, KIM W J. Annealing effects on the corrosion resistance of ultrafine-grained pure titanium [J]. Corrosion Science, 2014, 89: 331−337. DOI: https://doi.org/10.1016/j.corsci.2014.08.017.

[63] LIU Xing-yu, CHEN Si-yu, ZHANG Jin-jun, YANG Guang, ZHANG Ying, WANG Tao, LEI Jian-bo. Enhancement of the electrochemical corrosion resistance of Ti6Al4V alloy reinforced by nano- and micro-TiC particles through directed

energy deposition [J]. Corrosion Science, 2023, 221: 111343. DOI: https://doi.org/10.1016/j.corsci.2023.111343.
[64] CHIU Tse-ming, MAHMOUDI M, DAI Wei, ELWANY A, LIANG Hong, CASTANEDA H. Corrosion assessment of Ti−6Al−4V fabricated using laser powder-bed fusion additive manufacturing [J]. Electrochimica Acta, 2018, 279: 143−151. DOI: https://doi.org/10.1016/j.electacta.2018.04.189.

激光重熔对激光粉末床熔融 Ti6Al4V 钛合金显微组织和性能的影响

刘月洋[1]，杨 扬[1]，陈 翔[2]，詹宇星[1]

1. 中南大学 材料科学与工程学院，长沙 410083；
2. 江汉大学 精密爆破国家重点实验室，武汉 430056

摘 要：采用激光重熔工艺对激光粉末床熔融制备的 Ti6Al4V 钛合金进行后处理。光学显微镜、扫描电镜和电子背散射衍射观察表明，熔化区晶粒转变为平均尺寸为 1.31 μm 的等轴晶，热影响区晶粒得到细化。熔化区以及热影响区织构强度分别从原始激光粉末床熔融制备钛合金的 13.86 降低为 6.35 和 10.79。在激光重熔过程中，当激光扫描速度降低到一定程度时，温度梯度与凝固速率的比值减小，有效改善了激光粉末床熔融制备的 Ti6Al4V 合金的高择优取向，填充了表面孔洞缺陷。激光重熔处理提高了激光粉末床熔融工艺制备试样的硬度、耐磨性和耐腐蚀性。

关键词：激光粉末床熔融；激光重熔；晶粒细化；择优取向；磨损行为；电化学性能；Ti6Al4V

(Edited by Bing YANG)